Substrate Polarization Alters the Jahn-Teller Effect in a Single Molecule

Moritz Frankerl,[1,2,*] Laerte L. Patera,[3,4] Felix Giselbrecht,[3] Thomas Frederiksen,[2,5] Jascha Repp,[3,†] and Andrea Donarini[1,‡]

[1]*Institute for Theoretical Physics, University of Regensburg, 93040 Regensburg, Germany*
[2]*Donostia International Physics Center (DIPC), E-20018 Donostia-San Sebastián, Spain*
[3]*Institute for Experimental Physics, University of Regensburg, 93040 Regensburg, Germany*
[4]*Department of Physical Chemistry, University of Innsbruck, 6020 Innsbruck, Austria*
[5]*IKERBASQUE, Basque Foundation for Science, E-48013 Bilbao, Spain*

(Received 2 August 2024; revised 4 March 2025; accepted 27 March 2025; published 29 April 2025)

Charge-state transitions of a single Cu-phthalocyanine molecule adsorbed on an insulating layer of NaCl on Cu(111) are probed by means of alternate charging scanning tunneling microscopy. Real-space imaging of the electronic transitions reveals the Jahn-Teller distortion occurring upon formation of the first and second anionic charge states. The experimental findings are rationalized by a theoretical many-body model that highlights the crucial role played by the substrate. The latter enhances and stabilizes the intrinsic Jahn-Teller distortion of the negatively charged molecule hosting a degenerate pair of single-particle frontier orbitals. Consequently, two excess electrons are found to occupy, in the ground state, the same localized orbital, despite a larger Coulomb repulsion than the one for the competing delocalized electronic configuration. Control over the charging sequence by varying the applied bias voltage is also predicted.

DOI: 10.1103/PhysRevLett.134.176203

Scanning tunneling microscopy (STM) is an excellent tool for investigating single molecules on surfaces, as it combines atomic-scale imaging with spectroscopy. The hindrance of hybridization with the underlying metal achieved by ultrathin polar insulating films of 2–3 monolayers (ML) has been used to access near pristine electronic structures of molecules [1], many-body correlations [2,3], charge-state lifetimes [4], coherent spin control [5], and bistability between π-diradical open- and closed-shell states [6]. Furthermore it enabled the demonstration of fluorescence [7,8], vibronic spectroscopy [9], electrofluorochromism [10], and switching of the excitonic state [11] in single molecules as well as energy transfer in molecular dimers [12,13]. With few exceptions, investigating multiple charge states requires inhibiting electron exchange with the underlying substrate and, hence, working on thicker insulating films (> 20 ML), for which conventional STM is not applicable. Steering electron transfer with the tip and probing this transfer with atomic force microscopy (AFM) provides access to multiple charge states [14–16] and has enabled the study of single-electron transfer between molecules [17,18], reorganization energy upon charging [19], and excited molecular states and their lifetimes [20,21].

Alternate charging scanning tunneling microscopy (AC-STM) makes use of this development. In AC-STM single electrons are periodically tunneled back and forth between tip and molecule and detected *via* AFM. The signal represents the tunneling probability and can be used to spatially map different charge-state transitions [22–24]. The use of polar insulators in scanning probe microscopy leads to a strong stabilization of excess charges in adsorbed atoms and molecules [15,16,24–28]. It also facilitates orbital localization through self-trapping of polarons [29,30], thus revealing that the insulator's influence reaches beyond mere charge stabilization.

Here, we show how substrate polarization alters the Jahn-Teller (JT) effect in a charged Cu-phthalocyanine (CuPc) molecule. While the JT effect is well studied for singly charged CuPc, AC-STM reveals that charging with a second electron does not restore the original degeneracy of orbitals but instead leads to a double occupancy of one of the formerly degenerate orbitals. Our theoretical analysis reveals that the polarizable NaCl substrate does not only strongly enhance the JT splitting, but leads to a qualitatively different behavior for the dianionic species by tipping the energy balance. Moreover, we predict the transition rate to be dominated by the delocalized configuration at higher bias due to state multiplicity.

Experiments—We employ AC-STM [Fig. 1(a)] (cf. Supplemental Material (SM) [31] for details; see also

*Contact author: moritz.frankerl@dipc.org
†Contact author: jascha.repp@ur.de
‡Contact author: andrea.donarini@ur.de

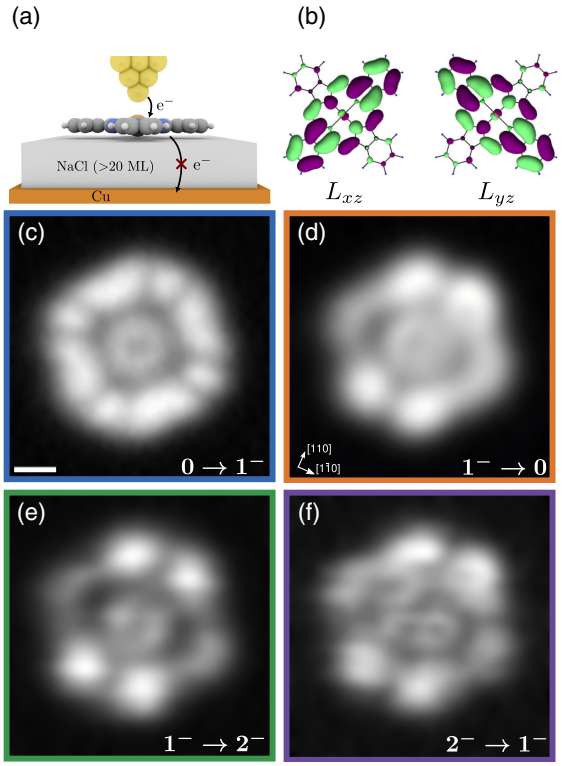

FIG. 1. (a) Sketch of the experimental setup. On thick NaCl films (> 20 ML), tunneling from the CuPc molecule to the Cu substrate is inhibited, enabling charge-state manipulation and the visualization of electronic transitions via AC-STM. (b) Isosurfaces of the two degenerate lowest unoccupied molecular orbitals (LUMOs) present in CuPc. (c)–(f) AC-STM images (oscillation amplitude $A = 1$ Å) corresponding to: (c) $0 \rightarrow 1^-$ transition ($V_{dc} = 1.0$ V, $V_{ac} = 0.75$ V peak-to-peak (V_{pp}), $\Delta z = 3.7$ Å) (d) $1^- \rightarrow 0$ transition ($V_{dc} = 1.0$ V, $V_{ac} = 1.0$ V_{pp}, $\Delta z = 4.4$ Å) (e) $1^- \rightarrow 2^-$ transition ($V_{dc} = 2.3$ V, $V_{ac} = 0.9$ V_{pp}, $\Delta z = 4.8$ Å) (f) $2^- \rightarrow 1^-$ transition ($V_{dc} = 2.3$ V, $V_{ac} = 1.0$ V_{pp}, $\Delta z = 4.0$ Å) Δz are given with respect to an AFM set point of $\Delta f = -1.5$ Hz at $V_{dc} = 0$ V. Scale bar: 5 Å. (a), (c), and (d) Reprinted figures with permission from Ref. [23]. Copyright 2019 by the American Physical Society.

Ref. [32] therein) to image the spatial distribution of charge-state transitions for the neutral, anionic, and dianionic CuPc species. To the substrate a dc voltage V_{dc} is applied, corresponding to the degeneracy point of the desired charge-state transition. Superimposed voltage pulses V_{ac} drive the charge-state transitions [22–24]. The map of the $0 \rightarrow 1^-$ transition [Fig. 1(c)] exhibits a fourfold rotational symmetry, similar to the anionic resonance observed by STM on ultrathin NaCl layers (2 ML) [27]. Additional back and forth toggling of the molecule's azimuthal orientation yields, on average, the superposition of two images rotated about 32° with respect to each other [23,33]. As reported previously [23], for the reverse transition ($1^- \rightarrow 0$) [Fig. 1(d)] the symmetry reduces from four to twofold due to the JT distortion, which favors in the anion the occupation of one single LUMO [27]. Expanding on previous studies we investigate here also the dianionic CuPc.

In the dianionic ground state the second excess electron could either occupy the other (empty) LUMO or further populate the already occupied one. The JT distortion lowers the energy of the already occupied orbital and thus pushes the system toward having two electrons in the already occupied LUMO. However, as can already be estimated from the LUMO densities in Fig. 1(b) the Coulomb repulsion will be higher for two electrons in one LUMO with respect to electrons being distributed between the LUMOs. Comparing the AC-STM images of the $1^- \rightarrow 2^-$ and $2^- \rightarrow 1^-$ transitions, displayed respectively in Figs. 1(e) and 1(f), with the one for the $1^- \rightarrow 0$ transition in Fig. 1(d), reveals that the second excess electron occupies the same orbital as the first one (see nodal-plane orientation). Statistical validation and additional datasets are provided in SM [31]. The intrinsic molecular Jahn-Teller, though, is insufficient to explain this result, as explained by the following theoretical analysis.

Model—We model the molecule in the AC-STM with the Hamiltonian

$$\hat{H} = \hat{H}_{mol} + \hat{H}_{tip} + \hat{H}_{tun} + \hat{H}_{as} + \hat{H}_{vib} + \hat{H}_{e\text{-}ph}, \quad (1)$$

where the minimal electronic description of the molecule (mol), metallic tip (tip) and tunneling coupling (tun) is complemented by a small environmental asymmetry (as), the set of molecular and substrate vibrational modes (vib), and by their coupling to the electronic degrees of freedom (e-ph). We write the molecular Hamiltonian in the Fock space of the four frontier orbitals, which are the singly occupied molecular orbital (S), the highest occupied molecular orbital (H) and the two degenerate LUMOs (L_{xz} and L_{yz}). The latter two are shown in Fig. 1(b). For more details on the modeling of the molecule, tip, and tunneling part of the Hamiltonian, we refer to SM [31] and our previous publications [34–38]. Additionally, we incorporate an environmental asymmetry via $\hat{H}_{as} = -\delta_{as}(\hat{n}_{xz} - \hat{n}_{yz})$, with $\delta_{as} = 4k_BT = 2$ meV into our model.

The vibronic Hamiltonian is a collection of harmonic oscillators $\hat{H}_{vib} = \sum_\zeta \hbar\omega_\zeta(\hat{a}_\zeta^\dagger \hat{a}_\zeta + ½)$ containing molecular and salt modes. Based on symmetry considerations, the vibrational modes of the system fall into three categories: (i) those not interacting with charges in the molecule, (ii) those affecting both LUMOs in the same way, and (iii) those interacting differently with each of the LUMOs. The C_{4v} symmetry of the combined salt and molecular system facilitates this classification (cf. SM [31] for more details on the treatment of the modes). We ignore the modes in the first category. The ones constituting the second category stabilize charge states in the molecule. They transform as the A_1 irreducible representation. We call them symmetric (S) since they do not reduce the symmetry

of the system. They are only sensitive to the global charge on the LUMOs, thus

$$\hat{H}^{\mathrm{S}}_{\text{e-ph}} = \sum_{\alpha \in \{A_1\}} g_\alpha (\hat{n}_{xz} + \hat{n}_{yz})(\hat{a}^\dagger_\alpha + \hat{a}_\alpha). \tag{2}$$

The modes in the third category affect the charge distribution within a specific charge state. We refer to them as antisymmetric (AS) modes, since they lower the symmetry of the molecule. They belong to the B_1 or B_2 irreducible representations. Because of energetic considerations (cf. SM [31]) we completely neglect the B_2 modes. The antisymmetric (B_1) modes couple to the imbalance between the populations of the L_{xz} and L_{yz} orbitals, i.e.,

$$\hat{H}^{\mathrm{AS}}_{\text{e-ph}} = \sum_{\beta \in \{B_1\}} g_\beta (\hat{n}_{xz} - \hat{n}_{yz})(\hat{a}^\dagger_\beta + \hat{a}_\beta). \tag{3}$$

We calculated the molecular mode energies as well as the corresponding electron-phonon couplings $g_{\alpha/\beta}$ from first principles using Inelastica [39,40], thus obtaining 14 symmetric (A_1) and 14 antisymmetric (B_1) modes (see SM for details [31]). The coupled salt modes can be combined to obtain just a single symmetric (A_1) and a single antisymmetric (B_1) mode. We take the corresponding electron-phonon couplings as free parameters in our theory and set them to $g^{\text{salt}}_{A_1} = 68$ meV and $g^{\text{salt}}_{B_1} = 40$ meV, assuming for the energy that of the transversal optical phonon mode $\hbar\omega_{\mathrm{TO}} = 20$ meV [41]. A microscopic derivation of this minimal model yielding coupling constants of comparable strength is given in SM [31]. We show a comparison between one symmetric molecular mode and the symmetric salt mode in Figs. 2(a) and 2(c). The antisymmetric case is displayed in Figs. 2(b) and 2(d). The influence of the symmetric modes on the many-body spectrum is obtained by a canonical Lang-Firsov transformation, leading to a renormalization of the single-particle energies $\tilde{\epsilon}_i = \epsilon_i - \sum_\alpha g^2_\alpha/\hbar\omega_\alpha$ as well as of the direct Coulomb interaction terms $\tilde{V}_{ijji} = V_{ijji} - 2\sum_\alpha g^2_\alpha/\hbar\omega_\alpha$ and $i, j \in \{L_{xz}, L_{yz}\}$. Thus, the energy renormalization induced by the symmetric salt mode explains the stabilization of charged molecules and atoms adsorbed on polar dielectrics due to the Franck-Condon blockade [42,43]. For antisymmetric modes, the exchange and pair hopping between LUMOs shows an intricate interplay with the electron-phonon coupling. In this case, the Lang-Firsov transformation does not eliminate the coupling between the electronic and the mechanical degrees of freedom, which persists in the transformed exchange and pair-hopping terms. We identify, instead, a single JT active mode and resort for our analysis into a semiclassical adiabatic approximation. To this end, we introduce the canonical displacement operators

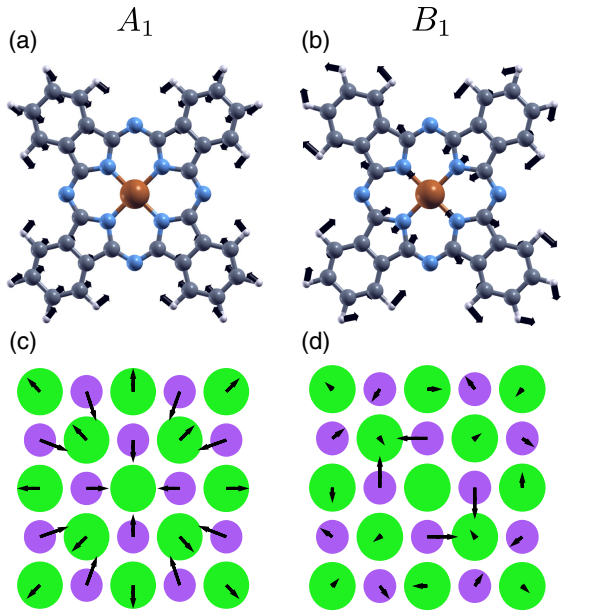

FIG. 2. (a),(b) Examples of an A_1 and a B_1 molecular vibrational mode, respectively (Cu in brown, C in gray, N in blue, H in white). (c),(d) In-plane displacement of the salt atoms (Cl^- in green, Na^+ in purple) corresponding to the A_1 (B_1) mode, respectively.

$$\hat{Q}_m = \sum_{\beta \in B_1} \sqrt{\hbar\omega_\beta}\, A_{m\beta}(\hat{a}^\dagger_\beta + \hat{a}_\beta), \tag{4}$$

where the first row of the transformation matrix reads $A_{1\beta} = (1/g)\sqrt{g^2_\beta/\hbar\omega_\beta}$ and yields the JT active mode $\hat{Q}_{\mathrm{AS}} \coloneqq \hat{Q}_1$. The JT distortion is thus described by the operator

$$\hat{H}_{\mathrm{JT}}(Q_{\mathrm{AS}}) = \frac{Q^2_{\mathrm{AS}}}{4} + g(\hat{n}_{xz} - \hat{n}_{yz})Q_{\mathrm{AS}}, \tag{5}$$

with Q_{AS} being the classical displacement of the JT active mode, with the effective coupling $g = \sqrt{\sum_\beta (g^2_\beta/\hbar\omega_\beta)}$. On this basis, we simulate the experimentally investigated many-body eigenstates and energies by diagonalizing the effective Hamiltonian

$$\hat{H}_{\mathrm{eff}} = \hat{\tilde{H}}_{\mathrm{mol}} + \hat{H}_{\mathrm{as}} + \hat{H}_{\mathrm{JT}}(Q_{\mathrm{AS}}) \tag{6}$$

along the coordinate Q_{AS} of the JT-active antisymmetric mode, with $\hat{\tilde{H}}_{\mathrm{mol}}$ containing the Lang-Firsov renormalization due to the symmetric modes.

Electronic structure—Some of the eigenenergies of $\hat{H}_{\mathrm{eff}}$ are the APESs plotted in Fig. 3. The lowest parabola in Fig. 3(d) is the APES of the neutral state. This neutral ground state defines the reference configuration ($Q_{\mathrm{AS}} = 0$). The anionic states with an excess electron in one of the

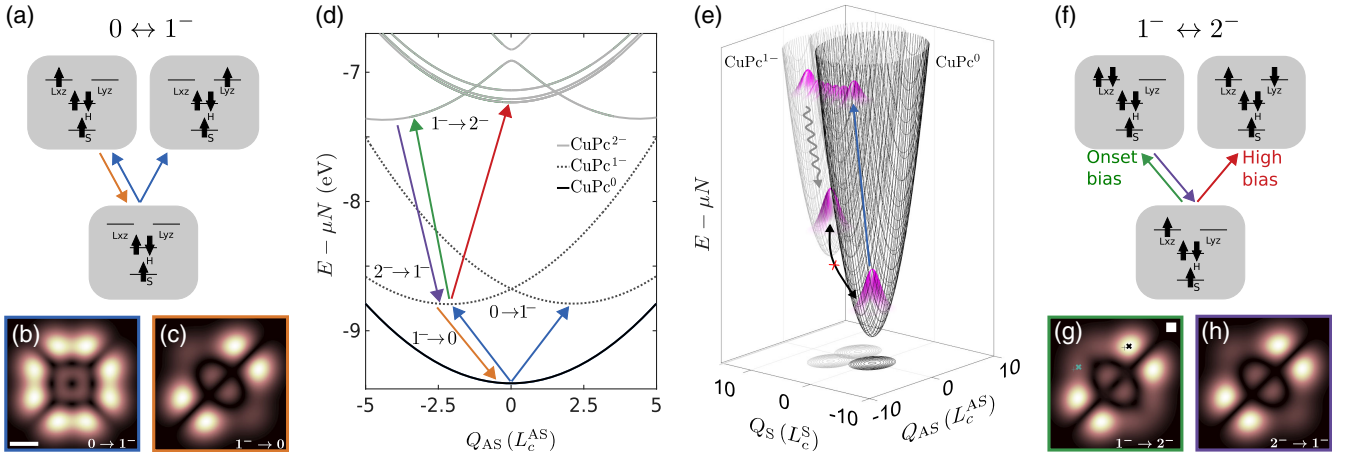

FIG. 3. Many-body states, energies, and transitions. (a) Many-body states relevant for the transitions between neutral and anionic states. (b) $0 \to 1^-$ at $V_b = 1.375$ V, shows fourfold symmetry. All scale bars are 5 Å and we use a Gaussian broadening of 4 Å. (c) $1^- \to 0$ at $V_b = 0.5$ V, fourfold symmetry is broken. (d) Adiabatic potential energy surfaces (APESs) as a function of the antisymmetric deformation coordinate (Q_{AS}). The arrows represent the transitions to the corresponding ground states at the energy given by APESs. (e) The $0 \to 1^-$ transition involves a strong excitation of the symmetric modes (Q_{S} coordinate) due to the large Huang-Rhys factor. The latter strongly suppresses the direct transition between ground states (black arrow). The allowed transition from the ground state to the vibronically excited state (blue arrow) is followed by the relaxation dynamics towards the vibrational ground state (wavy downward arrow). (f) Many-body states relevant for the transitions $1^- \leftrightarrow 2^-$. At a higher bias also the L_{yz} orbital is populated, as indicated by the red arrow. (g) $1^- \to 2^-$ at $V_b = 2.75$ V. At the onset bias the second added electron occupies the same L_{xz} orbital. The crosses indicate the positions reported in Fig. 4(a). (h) $2^- \to 1^-$ at $V_b = 1.8$ V.

LUMO levels are orbitally degenerate for $Q_{\mathrm{AS}} = 0$. Their energy is lowered upon deforming along Q_{AS}. Thus, the anionic ground state has one extra electron occupying the L_{xz} (L_{yz}) orbital for $Q_{\mathrm{AS}} < 0$ ($Q_{\mathrm{AS}} > 0$). The small environmental asymmetry δ_{as} ensures a global minimum with the excess electron in L_{xz}. The singlet-triplet splitting is not resolved on this energy scale. So far, the spectrum reflects the well-known JT effect. The richer structure of the dianionic APESs express two qualitatively different distributions of the excess electrons. For one excess electron in each of the L_{xz} and L_{yz} orbitals, the coupling to the JT mode vanishes. Thus, the lowest energy of these states (with different spin multiplicities) is found at $Q_{\mathrm{AS}} = 0$ in the upper part of Fig. 3(d). On the other hand, states with both excess electrons in the same former LUMO strongly couple to the JT mode. Their ground state is found at $Q_{\mathrm{AS}} \neq 0$, analogously to the anionic configuration, though with an even larger JT deformation and reorganization energy. Pair hopping between the real-valued orbitals induces the avoided crossing at $Q_{\mathrm{AS}} = 0$, characteristic of the pseudo JT effect [44].

Many-body transition rates—A qualitative understanding of the measured charge transitions is obtained by combining the electronic structure (detailed derivation in SM [31]) with few other constraints imposed by the experimental setup. Specifically, in AC-STM a single electron is tunneled back and forth per cantilever oscillation cycle of 34 μs duration. Hence, the system thermalizes between consecutive tunneling events. Moreover, the spectral broadening induced by the symmetric modes is much larger than the environmental asymmetry, which in turn exceeds the temperature. Those premises imply a fourfold symmetric neutral to anionic transition; it resembles the (incoherent) superposition of the L_{xz} and L_{yz} orbitals (with additional toggling), as it involves the spectrally unresolved states associated to both local minima with $Q_{\mathrm{AS}} > 0$ and $Q_{\mathrm{AS}} < 0$ [Figs. 1(c) and 3(b)]. In contrast, environmental asymmetry ensures, for the thermalized anion, the predominant occupation of the state with $Q_{\mathrm{AS}} < 0$; consequently the anionic to neutral transition acquires the twofold rotational symmetry of the L_{xz} orbital [Figs. 1(d) and 3(c)]. Mere energetic arguments would predict also for the transition between the anion and the dianion the participation of the states corresponding to both the deformed local minima in the dianionic APES. Single electron tunneling, though, forbids the contribution of the state with $Q_{\mathrm{AS}} > 0$ and double occupation of the L_{yz} orbital, and ultimately yields a many-body transition resembling again L_{xz} [Figs. 1(e) and 3(g)]. The same appearance is expected for the transition from the dianionic to the anionic ground state [Fig. 3(h)], although quantum fluctuations in the configuration of the dianion do not completely exclude small contributions from the L_{yz} orbital [cf. Fig. 1(f) and the SM [31] for dependence of the dianionic ground state on the deformation coordinate]. Electron tunneling implies displacements of both symmetric and antisymmetric modes. Their interplay is visualized in Fig. 3(e). The large electron-phonon coupling to the symmetric modes strongly suppresses the transitions between ground states along the effective symmetric

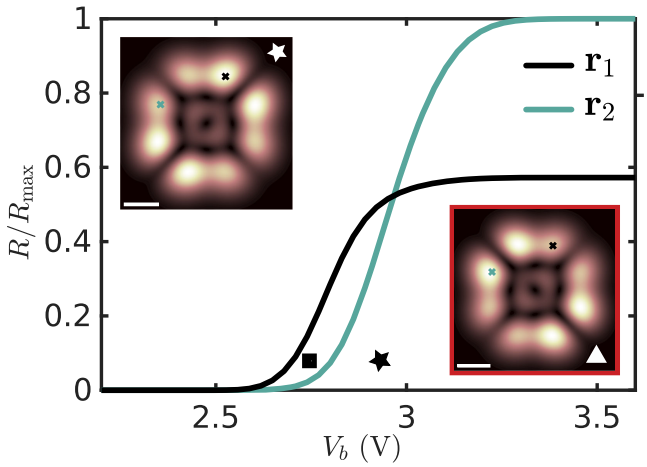

FIG. 4. Bias dependence of the anionic to dianionic transition rate calculated in two different positions. The rates are given as a fraction of the maximum calculated value $R_{\max}$. The ratio between the rates varies with the bias due to the opening of a further transition at higher bias [Fig. 2(f)]. The insets depict maps of the transition rate. The crosses mark the $\boldsymbol{r}_1$ and $\boldsymbol{r}_2$ positions used in the main figure. Star: calculated at $V_b = 2.9$ V. Triangle: map of the transition rate calculated at $V_b = 3.5$ V. At this bias the transition involving the L_{yz}-orbital is dominant [Fig. 2(g)]. Scale bar is 5 Å.

coordinate Q_S [black arrow in Fig. 3(e)]. On the contrary, with respect to the antisymmetric modes, transitions between ground states are possible. This phenomenon, visualized for the neutral to anionic transition holds for all other considered transitions between states with different charges. The theoretical transition maps in Figs. 3 and 4 are calculated with Fermi's golden rule as described in the End Matter. The tunneling rates are depicted in Fig. 3 as a function of the tip position and show a strong similarity to the experimental results, with also a remarkable agreement between all the experimental and theoretical transition voltages.

We notice, in this respect, that the 1^- to 2^- transition denoted with a green arrow in Fig. 3 is calculated, in accordance to the experiment, at the *onset* of the anion to dianion transition ($V_b = 2.75$ V). At higher biases we expect to open also transitions to the excited dianionic states, as sketched by the red arrows in Figs. 3(d) and 3(f). The bias dependence of the transition rate is shown in Fig. 4. We evaluate it in the tip positions visualized by the black and teal crosses in the insets. They select tunneling events involving a single orbital, respectively L_{xz} for $\boldsymbol{r}_1$ and L_{yz} for $\boldsymbol{r}_2$. The form of the dianionic ground state determines the lower bias onset for the rate in position $\boldsymbol{r}_1$. At a higher bias voltages both rates saturate, with the one at $\boldsymbol{r}_2$ being twice as large as the one at $\boldsymbol{r}_1$: the unoccupied orbital offers two spin channels as compared to the single one for an orbital already occupied by one electron. The predicted change of the full rate map is shown in the insets of Fig. 4. The comparison to Figs. 3(g) and 1 shows the emergence of the orthogonal LUMO (L_{yz} in our model) with an overall stronger signal [45]. Control over the landscape of the dianionic APES should also be obtained by changing the underlying salt. It is experimentally known that RbI, NaCl, and LiF have increasing influence onto the spectral broadening of molecular electronic states [46,47] and thus on the reorganization energy of the symmetric modes. We hypothesize a similar trend also for the antisymmetric modes, with a possible reversal of the orbital occupation sequence of CuPc on RbI with respect to the one on NaCl and LiF.

Conclusions—We have shown how the electron-phonon coupling between a charged molecule and the underlying substrate phonons determines the specific charge configuration within a molecule going beyond mere charge stabilization. We extend to this respect existing observations of charge localization in oligophenylene [24] and pentacene [28] to systems with JT distortion. Generally, we predict that the salt substrate has a larger effect on molecules with orbital degeneracy. This approach could pave the way to control charge configurations in molecules depending on the used substrate, with potential relevance in the study of intermolecular electron transfer, surface chemical reactivity, and charge sensing. We also envision the interplay between JT distortion of neighboring molecules for the realization of cellular automata based on molecular arrays in which the information is locally stored in the charge configuration of a single molecule.

Acknowledgments—We thank Luisa Raischl for the experimental support, moreover, we gratefully acknowledge financial support from the Deutsche Forschungsgemeinschaft (DFG, German Research Foundation) within Project-ID 314695032—SFB 1277 and RE2669/6-2, the ERC Synergy Grant MolDAM (No. 951519), the Spanish MCIN/AEI/10.13039/501100011033 (PID2020-330115406-GB-I00 and PID2023-146694NB-I00), the Basque Department of Education (PIBA-2023-1-0021), and the Euskampus Transnational Common Laboratory *QuantumChemPhys*.

[1] J. Repp, G. Meyer, S. M. Stojković, A. Gourdon, and C. Joachim, Molecules on insulating films: Scanning-tunneling microscopy imaging of individual molecular orbitals, Phys. Rev. Lett. **94**, 026803 (2005).
[2] F. Schulz, M. Ijäs, R. Drost, S. K. Hämäläinen, A. Harju, A. P. Seitsonen, and P. Liljeroth, Many-body transitions in a single molecule visualized by scanning tunnelling microscopy, Nat. Phys. **11**, 229 (2015).
[3] P. Yu, N. Kocić, J. Repp, B. Siegert, and A. Donarini, Apparent reversal of molecular orbitals reveals entanglement, Phys. Rev. Lett. **119**, 056801 (2017).
[4] K. Kaiser, L.-A. Lieske, J. Repp, and L. Gross, Charge-state lifetimes of single molecules on few monolayers of NaCl, Nat. Commun. **14**, 4988 (2023).

[5] P. Willke, T. Bilgeri, X. Zhang, Y. Wang, C. Wolf, H. Aubin, A. Heinrich, and T. Choi, Coherent spin control of single molecules on a surface, ACS Nano **15**, 17959 (2021).
[6] S. Mishra, M. Vilas-Varela, L.-A. Lieske, R. Ortiz, S. Fatayer, I. Rončević, F. Albrecht, T. Frederiksen, D. Peña, and L. Gross, Bistability between π-diradical open-shell and closed-shell states in indeno[1,2-a]fluorene, Nat. Chem. **16**, 755 (2024).
[7] X. H. Qiu, G. V. Nazin, and W. Ho, Vibrationally resolved fluorescence excited with submolecular precision, Science **299**, 542 (2003).
[8] L. Zhang, Y.-J. Yu, L.-G. Chen, Y. Luo, B. Yang, F.-F. Kong, G. Chen, Y. Zhang, Q. Zhang, Y. Luo, J.-L. Yang, Z.-C. Dong, and J. G. Hou, Electrically driven single-photon emission from an isolated single molecule, Nat. Commun. **8**, 580 (2017).
[9] B. Doppagne, M. C. Chong, E. Lorchat, S. Berciaud, M. Romeo, H. Bulou, A. Boeglin, F. Scheurer, and G. Schull, Vibronic spectroscopy with submolecular resolution from STM-induced electroluminescence, Phys. Rev. Lett. **118**, 127401 (2017).
[10] B. Doppagne, M. C. Chong, H. Bulou, A. Boeglin, F. Scheurer, and G. Schull, Electrofluorochromism at the single-molecule level, Science **361**, 251 (2018).
[11] J. Doležal, P. Mutombo, D. Nachtigallová, P. Jelínek, P. Merino, and M. Švec, Mechano-optical switching of a single molecule with doublet emission, ACS Nano **14**, 8931 (2020).
[12] H. Imada, K. Miwa, M. Imai-Imada, S. Kawahara, K. Kimura, and Y. Kim, Real-space investigation of energy transfer in heterogeneous molecular dimers, Nature (London) **538**, 364 (2016).
[13] S. Cao, A. Rosławska, B. Doppagne, M. Romeo, M. Féron, F. Chérioux, H. Bulou, F. Scheurer, and G. Schull, Energy funnelling within multichromophore architectures monitored with subnanometre resolution, Nat. Chem. **13**, 766 (2021).
[14] E. Bussmann and C. C. Williams, Single-electron tunneling force spectroscopy of an individual electronic state in a nonconducting surface, Appl. Phys. Lett. **88**, 263108 (2006).
[15] L. Gross, F. Mohn, P. Liljeroth, J. Repp, F. J. Giessibl, and G. Meyer, Measuring the charge state of an adatom with noncontact atomic force microscopy, Science **324**, 1428 (2009).
[16] W. Steurer, S. Fatayer, L. Gross, and G. Meyer, Probe-based measurement of lateral single-electron transfer between individual molecules, Nat. Commun. **6**, 8353 (2015).
[17] W. Steurer, J. Repp, L. Gross, I. Scivetti, M. Persson, and G. Meyer, Manipulation of the charge state of single au atoms on insulating multilayer films, Phys. Rev. Lett. **114**, 036801 (2015).
[18] P. Scheuerer, L. L. Patera, and J. Repp, Manipulating and probing the distribution of excess electrons in an electrically isolated self-assembled molecular structure, Nano Lett. **20**, 1839 (2020).
[19] S. Fatayer, B. Schuler, W. Steurer, I. Scivetti, J. Repp, L. Gross, M. Persson, and G. Meyer, Reorganization energy upon charging a single molecule on an insulator measured by atomic force microscopy, Nat. Nanotechnol. **13**, 376 (2018).
[20] S. Fatayer, F. Albrecht, I. Tavernelli, M. Persson, N. Moll, and L. Gross, Probing molecular excited states by atomic force microscopy, Phys. Rev. Lett. **126**, 176801 (2021).
[21] J. Peng, S. Sokolov, D. Hernangómez-Pérez, F. Evers, L. Gross, J. M. Lupton, and J. Repp, Atomically resolved single-molecule triplet quenching, Science **373**, 452 (2021).
[22] L. L. Patera, F. Queck, P. Scheuerer, and J. Repp, Mapping orbital changes upon electron transfer with tunnelling microscopy on insulators, Nature (London) **566**, 245 (2019).
[23] L. L. Patera, F. Queck, P. Scheuerer, N. Moll, and J. Repp, Accessing a charged intermediate state involved in the excitation of single molecules, Phys. Rev. Lett. **123**, 016001 (2019).
[24] L. L. Patera, F. Queck, and J. Repp, Imaging charge localization in a conjugated oligophenylene, Phys. Rev. Lett. **125**, 176803 (2020).
[25] J. Repp, G. Meyer, F. E. Olsson, and M. Persson, Controlling the charge state of individual gold adatoms, Science **305**, 493 (2004).
[26] S. W. Wu, N. Ogawa, G. V. Nazin, and W. Ho, Conductance hysteresis and switching in a single-molecule junction, J. Phys. Chem. C **112**, 5241 (2008).
[27] C. Uhlmann, I. Swart, and J. Repp, Controlling the orbital sequence in individual Cu-phthalocyanine molecules, Nano Lett. **13**, 777 (2013).
[28] D. Hernangómez-Pérez, J. Schlör, D. A. Egger, L. L. Patera, J. Repp, and F. Evers, Reorganization energy and polaronic effects of pentacene on NaCl films, Phys. Rev. B **102**, 115419 (2020).
[29] B. Li, J. Zhao, K. Onda, K. D. Jordan, J. Yang, and H. Petek, Ultrafast interfacial proton-coupled electron transfer, Science **311**, 1436 (2006).
[30] M. Setvin, C. Franchini, X. Hao, M. Schmid, A. Janotti, M. Kaltak, C. G. Van de Walle, G. Kresse, and U. Diebold, Direct view at excess electrons in TiO_2 rutile and anatase, Phys. Rev. Lett. **113**, 086402 (2014).
[31] See Supplemental Material at http://link.aps.org/supplemental/10.1103/PhysRevLett.134.176203 for statistical validation and further experimental and theoretical details.
[32] F. J. Giessibl, Atomic resolution on Si(111)-(7 × 7) by noncontact atomic force microscopy with a force sensor based on a quartz tuning fork, Appl. Phys. Lett. **76**, 1470 (2000).
[33] K. Miwa, H. Imada, S. Kawahara, and Y. Kim, Effects of molecule-insulator interaction on geometric property of a single phthalocyanine molecule adsorbed on an ultrathin NaCl film, Phys. Rev. B **93**, 165419 (2016).
[34] S. Sobczyk, A. Donarini, and M. Grifoni, Theory of STM junctions for π-conjugated molecules on thin insulating films, Phys. Rev. B **85**, 205408 (2012).
[35] A. Donarini, B. Siegert, S. Sobczyk, and M. Grifoni, Topographical fingerprints of many-body interference in STM junctions on thin insulating films, Phys. Rev. B **86**, 155451 (2012).
[36] B. Siegert, A. Donarini, and M. Grifoni, Effects of spin-orbit coupling and many-body correlations in STM transport through copper phthalocyanine, Beilstein J. Nanotechnol. **6**, 2452 (2015).
[37] B. Siegert, A. Donarini, and M. Grifoni, Nonequilibrium spin crossover in copper phthalocyanine, Phys. Rev. B **93**, 121406(R) (2016).

[38] M. Frankerl and A. Donarini, Spin-orbit interaction induces charge beatings in a lightwave-STM—single molecule junction, Phys. Rev. B **103**, 085420 (2021).
[39] J. M. Soler, J. M. Artacho, J. D. Gale, A. García, J. Junquera, P. Ordejón, and D. Sánchez-Portal, The SIESTA method for *ab initio* order-*N* materials simulation, J. Phys. Condens. Matter **14**, 2745 (2002).
[40] T. Frederiksen, M. Paulsson, M. Brandbyge, and A.-P. Jauho, Inelastic transport theory from first principles: Methodology and application to nanoscale devices, Phys. Rev. B **75**, 205413 (2007).
[41] G. Raunio and S. Rolandson, Lattice dynamics of NaCl, KCl, RbCl, and RbF, Phys. Rev. B **2**, 2098 (1970).
[42] A. Mitra, I. Aleiner, and A. J. Millis, Phonon effects in molecular transistors: Quantal and classical treatment, Phys. Rev. B **69**, 245302 (2004).
[43] J. Koch, F. von Oppen, and A. V. Andreev, Theory of the Franck–Condon blockade regime, Phys. Rev. B **74**, 205438 (2006).
[44] I. B. Bersuker, *The Jahn-Teller Effect* (Cambridge University Press, Cambridge, England, 2006).
[45] Additional measurements taken during the review process seem to confirm this theoretical prediction.
[46] J. Repp and G. Meyer, Scanning tunneling spectroscopy of molecules on insulating films, Chimia **64**, 370 (2010).
[47] N. Pavliček, I. Swart, J. Niedenführ, G. Meyer, and J. Repp, Symmetry dependence of vibration-assisted tunneling, Phys. Rev. Lett. **110**, 136101 (2013).
[48] J. Repp, G. Meyer, S. Paavilainen, F. E. Olsson, and M. Persson, Scanning tunneling spectroscopy of Cl vacancies in NaCl films: Strong electron-phonon coupling in double-barrier tunneling junctions, Phys. Rev. Lett. **95**, 225503 (2005).

End Matter

Methods—The transition rate from an initial thermalized state toward a vibrationally excited state with neighboring charge reads

$$R^{N\to N+1} = \sum_{\{n_\alpha\},f} \sum_{i,j,\sigma} \prod_{\alpha\in\{A_1\}} \Gamma_{i\sigma,j\sigma}(\boldsymbol{r}_{\mathrm{tip}}) P_{\lambda_\alpha}(\{n_\alpha\}) f^+(E_f - E_g - ecV_b) \langle N+1, f|\hat{d}^\dagger_{i\sigma}|N, g\rangle\langle N, g|\hat{d}_{j\sigma}|N+1, f\rangle, \quad \text{(A1a)}$$

$$R^{N+1\to N} = \sum_{\{n_\alpha\},f} \sum_{i,j,\sigma} \prod_{\alpha\in\{A_1\}} \Gamma_{i\sigma,j\sigma}(\boldsymbol{r}_{\mathrm{tip}}) P_{\lambda_\alpha}(\{n_\alpha\}) f^-(E_g - E_f - ecV_b) \langle N+1, g|\hat{d}^\dagger_{i\sigma}|N, f\rangle\langle N, f|\hat{d}_{j\sigma}|N+1, g\rangle, \quad \text{(A1b)}$$

where the single-particle rate matrix is given by $\Gamma_{i\sigma,j\sigma}(\boldsymbol{r}_{\mathrm{tip}}) = (2\pi/\hbar)\sum_k t^*_{k,i\sigma} t_{k,j\sigma}\delta(E_f - E_g - \epsilon_k)$. The symmetric modes' Franck-Condon factors yield the Poisson distributions $P_{\lambda_\alpha}(\{n_\alpha\})$, which depend on the Huang-Rhys factors $\lambda_\alpha = (g_\alpha/\hbar\omega_\alpha)$ and $\{n_\alpha\}$ is the set of the final state's vibrational excitations with respect to all modes $\alpha\in\{A_1\}$. Because of the large electron-phonon coupling $\lambda_{\mathrm{salt}} \approx 5$, the salt contribution converges to a Gaussian and it is the main source of spectral broadening [48]. The Fermi function f^+ (and related $f^- = 1 - f^+$) with the tip temperature $T = 6$ K and chemical potential $\mu = -4.65$ eV is calculated at the difference between the molecular many-body energies shifted by the fraction $c = 0.6$ of sample bias V_b dropping between the molecule and the tip. The energy of the final state $E_f = E^e_f + \sum_\alpha \hbar\omega_\alpha n_\alpha$ includes the electronic potential energy E^e_f (the local minima of the APES in Fig. 3) and the excitation energies of the symmetric modes, while E_g is the ground state energy of the initial state. Finally, Eqs. (A1a) and (A1b) include the transition matrix elements between different charge states. To this end, we denote the initial state with $|N, g\rangle$ ($|N+1, g\rangle$) and the final state with $|N+1, f\rangle$ ($|N, f\rangle$). The sum over f extends to all possible states accessible from the designated initial state via a single electron tunneling event.